We are IntechOpen, the world's leading publisher of Open Access books Built by scientists, for scientists

4,800
Open access books available

122,000
International authors and editors

135M
Downloads

Our authors are among the

154
Countries delivered to

TOP 1%
most cited scientists

12.2%
Contributors from top 500 universities

WEB OF SCIENCE™

Selection of our books indexed in the Book Citation Index in Web of Science™ Core Collection (BKCI)

Interested in publishing with us?
Contact book.department@intechopen.com

Numbers displayed above are based on latest data collected.
For more information visit www.intechopen.com

3

A Frequency Domain Systems Theory Perspective for Semiconductor Optical Amplifier - Mach Zehnder Interferometer Circuitry in Routing and Signal Processing Applications

George T. Kanellos[1], Maria Spyropoulou[2], Konstantinos Vyrsokinos[1], Amalia Miliou[2] and Nikos Pleros[2]
[1]*Informatics and Telematics Institute, Center for Research and Technology Hellas*
[2]*Department of Informatics, Aristotle University of Thessaloniki*
Greece

1. Introduction

1.1 SOAs as nonlinear elements in Mach-Zehnder Interferometers

Although SOAs have been initially introduced as integrated modules mainly for optical amplification purposes, they have been widely used in all optical signal processing applications, like all-optical switching and wavelength conversion, utilizing the exhibited nonlinearities such as gain saturation, cross-gain (XGM) and cross-phase modulation (XPM). These nonlinear effects that present the most severe problem and limit the usefulness of SOAs as optical amplifiers in lightwave systems can be proven attractive in optically transparent networks. The origin of the nonlinearities lies in the SOA gain saturation and in its correlation with the phase of the propagating wave, since the carrier density changes induced by the input signals are affecting not only the gain but also the refractive index in the active region of the SOA. The carrier density dynamics within the SOA are very fast (picosecond scale) and thus the gain responds in tune with the fluctuations in the input power on a bit by bit basis even for optical data at 10 or 40 Gb/s bit-rates (Ramaswami & Sivarajan, 2002).

If more than one signal is injected into the SOA, their nonlinear interaction will lead to XPM between the signals. However, in order to take advantage of the XPM phenomenon and create functional devices, the SOAs have to be placed in an interferometric configuration such as a Mach-Zehnder Interferometer (MZI) that converts phase changes in the signals to intensity variations at its output exploiting interference effects. Semiconductor Optical Amplifier-based Mach-Zehnder Interferometers (SOA-MZIs) have been widely used in the past years as all-optical high speed switches for signal conditioning and signal processing, mainly due to their low switching power requirements and their potential for integration (Maxwell, 2006). Using this type of switch, a set of processing operations ranging from demultiplexing (Duelk et al.,1999) to regeneration (Ueno et al., 2001) and wavelength

conversion (Nielsen et al. 2003) to optical sampling (Fischer et al. 2001) and optical flip-flops (Hill et al. 2001, Pleros et al. 2009) has been demonstrated, highlighting multi-functionality as an additional advantage of SOA-MZI devices. Within the same frame, SOA-MZI devices have proven very efficient in dealing with packet-formatted optical traffic allowing for their exploitation in several routing/processing demonstrations for optical packet or burst switched applications, performing successfully in challenging and demanding functionalities like packet envelope detection (Stampoulidis et al, 2007), packet clock recovery (Kanellos et al, 2007a), label/payload separation (Ramos et al, 2005), burst-mode reception (Kanellos et al, 2007a, 2007b) and contention resolution (Stampoulidis et al, 2007).A brief description of the most important SOA-MZI signal processing applications and their principle of operation is provided in the following paragraphs.

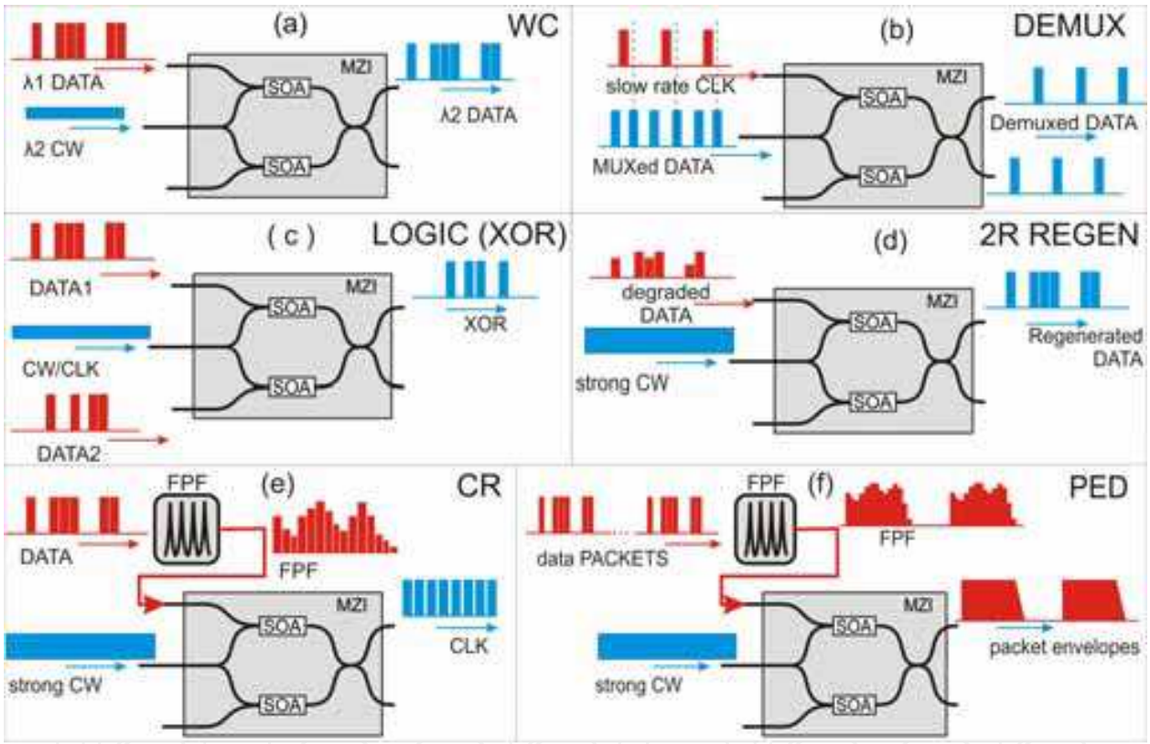

Fig. 1. Single MZI basic functionalities: a) wavelength conversion b) demultiplexing c) Boolean logic (XOR) operation d) 2R regeneration e) Clock recovery (CR) f) Packet envelope detection (PED)

1.1.1 Wavelength converters

An important class of application area for SOA-MZIs is wavelength conversion both for RZ and NRZ data formats, offering also 2R regenerative characteristics to the wavelength converted signal as a result of their nonlinear transfer function. Several schemes were developed during the decade of the 1990s (Durhuus et al. 1994), and many others have been proposed since then ((Stubkjaer, 2000; Wolfson et al. 2000; Leuthold, J. 2001; Nakamura et al. 2001; M. Masanovic et al. 2003; Apostolopoulos et al. 2009a).

Figure 1(a) depicts the standard WC layout employing a single control signal that is inserted into one of the two MZI arms causing a gain and phase variation only to one of the two CW

signal components. This configuration offers the advantage of reduced complexity but is liable to result in pulse broadening and significant patterning effects due to the unbalanced gain saturation in the two SOAs, severely limiting the operational speed of the device especially when NRZ pulses are used. In the case of RZ signal formats, unequal SOA gain-induced speed restrictions can be overcome by the well-known "push-pull" architecture that employs two identical control signal entering the two SOAs with a differential time delay. In the case of NRZ data format, these effects are partially compensated in the bidirectional push-pull scheme, which employs two identical control pulses travelling in opposite directions through the two MZI branches, while further improvement is achieved by the recently proposed Differentially-biased NRZ wavelength conversion scheme that provides enhanced 2R regenerative characteristics (Apostolopoulos et al. 2009a,b).

1.1.2 All-optical logic gates

The successful employment of SOA-MZIs in all-optical Boolean logic configurations has been the main reason for referring to SOA-MZIs as the all-optical version of the electronic transistor. All-optical logic gates based on SOA-MZI structures using cross phase modulation have demonstrated several interesting merits, i.e. high extinction ratio, regenerative capability, high speed of operation, and low chirp in addition to low energy requirement and integration capability. Particular attention has been paid to the all-optical XOR gate that forms a key technology for implementing primary systems for binary address and header recognition, binary addition and counting, pattern matching, decision and comparison, generation of pseudorandom binary sequences, encryption and coding. This gate has been demonstrated at 40 Gb/s (Webb et al. 2003) using SOA-MZI schemes. Figure 1 (c) presents the principle of Boolean XOR operation. Moreover, Kim et al. proposed and experimentally demonstrated all-optical multiple logic gates with XOR, NOR, OR, and NAND functions using SOA-MZI structures that enable simultaneous operations of various logic functions with high ER at high speed (Kim et al, 2005).

1.1.3 All- Optical 2R/3R regeneration

All–optical regeneration is employed at the input of an optical node in order to relieve the incoming data traffic from the accumulated signal quality distortions and to restore a high-quality signal directly in the optical domain prior continuing its route through the network. 2R regeneration generic layout comprises a SOA-MZI interferometer configured in wavelength conversion operation and powered with a strong CW signal. The saturated SOAs in combination with the interferometric transfer function of the gate exhibit a highly non-linear step-like response and the configuration operates as a power limiter (Pleros et al. 2004), forcing unequal power level pulses to equalization. SOA-MZIs have been usually utilized as the nonlinear regenerating elements in several optical 2R regeneration experiments up to 40Gb/s (Apostolopoulos et al,2009a). The block diagram of this setup is shown in Fig. 1(d). All–optical 3R regeneration combines the 2R regeneration module, acting as a decision element, with a clock recovery unit, an important subsystem that produces high-quality data-rate clock pulses. The decision element is used for imprinting the incoming data logical information onto the "fresh" clock signal. The clock recovery process has been demonstrated to perform with different length 40Gb/s asynchronous packets, using a low-Q FPF filter with a highly saturated SOA-MZI gate (Kanellos et al. 2007a). The block diagram setup of the clock recovery subsystem is shown in Fig. 1(e).

1.1.4 DEMUX and Add/Drop multiplexer

Demultiplexing and add/drop multiplexing have been among the first applications areas of SOA-MZI devices, successfully providing the required wavelength and/or data-rate adaptation at the node's front-end. The use of SOA-MZI configurations has initially been demonstrated for demultiplexing purposes from 40 to 10 Gbit/s (Duelk et al.,1999). Figure 1(b) presents the experimental set-up used for the demultiplexing operation.

1.1.5 Burst-Mode Receiver

Burst-mode reception (BMR) is a highly challenging yet necessary functionality on the way to optical packet and burst-mode switched networks, as it has to be capable of adapting to and handling arriving packets with different phase alignment and optical power levels, ensuring at the same time successful regeneration at the intermediate network nodes or error-free reception at the end-user terminals. SOA-MZI-based designs have been already presented in several 2R and 3R setups to simplify the BMR circuit design, whereas the interconnection of four cascaded SOA-MZI gates has led also to the first BMR architecture demonstrated at 40Gb/s (Kanellos et al. 2007a). Each one of the four SOA-MZI modules in this BMR setup provides a different functional task, namely wavelength conversion, power level equalization, clock recovery and finally regeneration or reception.

1.1.6 Optical RAM

Buffering and Random Access Memory (RAM) functionality have been the main weakness of photonic technologies compared to electronics, mainly due to the neutral charge of photon particles that impedes them to mimic the storage behavior of electrons. The first all-optical static RAM cell with true random access read/write functionality has been only recently feasible by exploiting a SOA-MZI-based optical flip-flop and two optically controlled SOA-based ON/OFF switches (Pleros et al. 2009), providing a proof-of-principle solution towards high-speed all-optical RAM circuitry. The optical flip-flop serves as the single-bit memory element utilizing the wavelength dimension and the coupling mechanism between the two SOA-MZIs for determining the memory content, whereas the two SOAs operate as XGM ON/OFF switches controlling access to the flip-flop configuration.

1.1.7 Contention resolution

Packet envelope detection is performed by extracting the envelope of the incoming optical packets (Figure 1(f)). All-optical PED has been demonstrated using an integrated SOA-MZI (Stampoulidis et al. 2007). In these experiments the PED circuit consists of a passive filter in combination with an SOA-MZI gate operated as a low-bandwidth 2R regenerator. The PED circuit generates a packet envelope, indicating the presence of a packet at the specific timeslot. The same experimental work has demonstrated contention resolution in the wavelength domain, using the PED signal to wavelength-convert the deflected packets (Stampoulidis et al. 2007).

1.2 Progress in fabrication and integration: technology overview

The large variety of signal processing and routing applications demonstrated during the last decade by means of SOA-MZI-based circuitry has been mainly a result of the remarkable progress in monolithic and hybrid photonic integration. This has allowed for increased integration densities at high-speed channel rates, offering at the same time the potential for

multiple SOA-MZI interconnection even in cascaded stages (Zakynthinos et al.2007, Apostolopoulos et al. 2009b), lower cost, smaller footprints and lower power consumption.
The silica-on-silicon hybrid integration platform developed by the Center for Integrated Photonics (CIP, U.K.) has been proven a technique of great potential, enabling flip-chip bonding of pre-fabricated InP and InGaAsP components, including SOAs and modulators, on silicon boards with low loss waveguides (Maxwell et al. 2006). This technique relies on the design and development of a planar silica waveguide acting as a motherboard, which is capable of hosting active and passive devices, similar to the electronic printed circuit board used in electronics. The active elements of the device are independently developed on precision-machined silicon submounts called "daughterboards." In the case of SOA-MZI development, the daughterboards are designed to host monolithic SOA chips and provide all suitable alignment stops. The daughterboard consists of a double SOA array and is flip chipped onto the motherboard. This platform has led also to the implementation of multielement photonic integrated circuits, paving the way towards true all-optical systems on-chip that can yield both packaging and fiber pig-tailing cost reduction while retaining cost effectiveness through a unified integration platform for a variety of all-optical devices. Toward this milestone, SOA_MZI regenerators integrated on the same chip with bandpass filtering elements have been shown to perform successfully in WDM applications (Maxwell et al. 2006), while high-level system applications have been demonstrated by making use of the first quadruple arrays of hybridly integrated SOA-MZI gates (Stampoulidis et al. 2008).
Monolithic integration has also witnessed significant progress, presenting Photonic Integrated Circuits (PICs) that incorporate several active and passive components, being capable of meeting different performance requirements on a single chip. A butt-joint growth-based integration platform was explored to incorporate both high- and low-confinement active regions in the same device. To this end, monolithically widely tunable all-optical differential SOA-MZI wavelength converter operating at 40Gb/s have been implemented (Lal et al. 2006), whereas the device functionality was extended by incorporating an electrical modulation stage yielding a monolithic Packet Forwarding Chip (PFC). These structures enabled the successful realization of three major high-rate packet switching functions in a single monolithic device, allowing for simultaneous tunability, all-optical wavelength conversion, and optical label encoding. Monolithic integration holds also the record number of more than 200 passive and active elements integrated on the same functional chip, leading to the first 8x8 InP monolithic tunable optical router capable of operating at 40-Gb/s (Nicholes et al. 2010).

1.3 Modeling and Theory approaches so far

Despite the significant progress in SOA-MZI-based applications and the maturity reached in this technology during the last years, its theoretical toolkit is still missing a holistic frequency domain analysis that will be capable of yielding a common basis for the qualitative understanding of all SOA-MZI enabled nonlinear functionalities. Although single SOAs have been extensively investigated using both time- and frequency-domain theoretical methods (Davies, 1995, Mørk et al.1999), SOA-MZI theory has mainly relied on time-domain simulation-based approaches (Melo et al. 2007) employing customized frequency-domain analytical methods only for specific applications (Kanellos et al 2007b). However, it is well-known from system's theory that a unified frequency-domain argumentation of the experimentally proven multifunctional potential of SOA-MZIs can allow for simple analytical procedures in the performance analysis of complex SOA-MZI-based setups, leading also to optimized configurations. The modulation bandwidth

enhancement of the SOA-based Delayed Interferometer Signal Converter (DISC) through chirp filtering (Nielsen et al 2004) and its associated subsequent applications are timely examples for the research strength that can be unleashed by a solid theoretical frequency domain model. This chapter aims to introduce a frequency-domain description of the SOA-MZI transfer function providing a solid system's theory platform for the analysis and performance evaluation of SOA-MZI circuitry. The following sections have been structured so as to introduce the mathematical framework required for the SOA-MZI transfer function extraction, to present its application in several SOA-MZI architectural designs and, finally, to use it in the analysis and evaluation of well-known complex SOA-MZI-based devices exploiting well-established system's theory procedures.

2. Theory development

2.1 SOA-MZI all-optical wavelength conversion generic layout

SOA-MZI all optical wavelength conversion is the fundamental operation for the interferometric devices, as it represents either a stand-alone key network application or an essential sub-system functionality to be employed in larger and more complicated processing systems. The principle of operation of the SOA-MZI AOWCs relies on splitting the injected CW input signal into two spatial components that propagate through the two MZI branches and are forced to interfere at the output coupler after experiencing the induced SOA carrier density changes and the associated cross-gain (XGM) and cross-phase modulation (XPM) phenomena imposed by the control signals. In this way, the optical data signal serving as the Control (CTR) signal into the SOA-MZI is imprinted onto the CW input beam, resulting to a replica of the inserted data sequence carried by a new wavelength and emerging at the Switched-port (S-port) of the MZI.

Fig. 2(a-c) illustrates all possible configurations of SOA-MZI-based wavelength converters and their principle of operation, with their classification being determined by the type of signals injected into the SOA-MZI. Fig. 2(a-c) illustrate the operation principle for each corresponding case. Fig. 2(d-f) show the amplitude and phase of the upper (x) and lower (y) cw components with the red solid line and the dotted lines, respectively, after passing through the SOA devices at the impulse of an NRZ pulse.

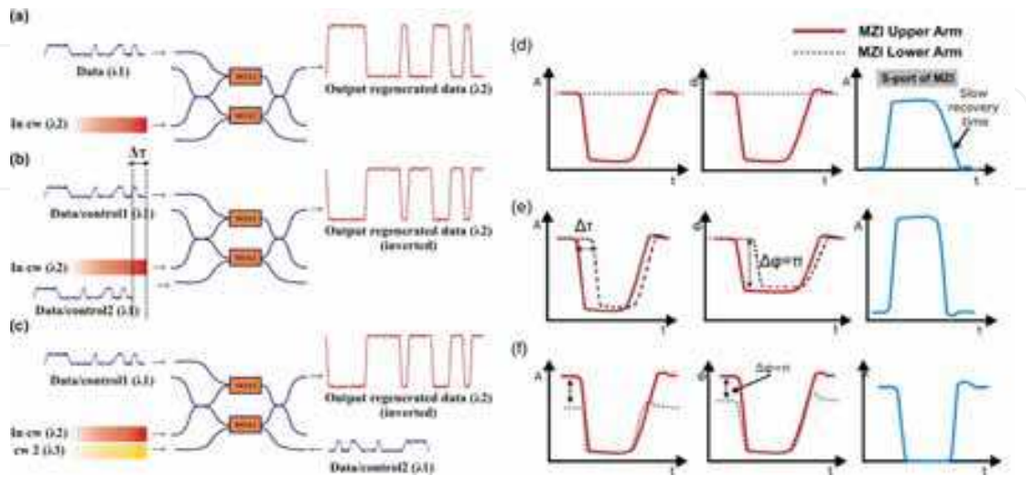

Fig. 2. Description of the SOA-MZI wavelength conversion configurations: (a) standard, (b) push-pull and (c) differentially biased.

To this end, Fig. 2(a) illustrates the simplest configuration called the standard SOA-MZI scheme, employing a strong continuous wave (CW) signal at λ_1 commonly inserted into both SOA-MZI branches after passing through the input 3 dB coupler. A weak data signal at λ_2 is inserted into the upper branch as the control (CTR_x) and is responsible for altering the gain and phase dynamics of the upper branch CW signal by stimulating the cross-gain (XGM) and cross-phase modulation (XPM) phenomena on the upper SOA. Finally, the two CW components traveling along the upper and lower SOA-MZI arms interfere constructively at the output 3 dB coupler, yielding the wavelength converted signal at the switched port. As shown in Fig.2(a), only the amplitude and phase of the upper CW component are affected (red line) due to the carrier modulation imposed by the input control pulse (CTR_x), whereas the amplitude and phase of the lower CW component remain constant (dotted line) and they are only subject to the waveguide propagation loss. The result of the interference between the two output CW components is the wavelength converted output signal shown at the top right corner, suffering though from slow rise and fall times due to the slow gain recovery time of the SOA. The second SOA-MZI wavelength conversion scheme is illustrated in Fig.2(b) and is called the PUSH PULL configuration. In this scheme, the control signal is split through a coupler and the two parts of the signal are fed as the control signals CTR_x and CTR_y of the upper and lower branches of the SOA-MZI after experiencing a differential time delay $\Delta\tau$. In this way, the gains of the two SOAs are suppressed at different time instances separated by Δt, while the optical powers of the controls signals may be adjusted properly in order to induce a differential phase shift close to π rad (Fig.2.b) for the time fraction that the optical pulses of the two control signals are not overlapping in time. The output wavelength converted signal is dominated by this differential phase shift and appears at the switched port of the SOA-MZI. The width of the output optical pulse is strongly dependent on the differential time delay $\Delta\tau$, while the rise and fall times are shorter compared to the standard operation since the symmetrical gain saturation at the upper and lower SOA-MZI arms cancels out the slow recovery time of the SOAs. The switching speed of the push-pull SOA-MZI configuration will increase as $\Delta\tau$ reduces and the switching window shrinks, enabling in this way high operational speeds. However, the requirement for $\Delta\tau$ delay between the two control signals enforces the availability of empty time durations within a single bit-slot, rendering this scheme suitable only for RZ optical pulses.

The differentially biased scheme illustrated in Fig. 2(c) employs again two identical control signals entering the respective MZI arms, enabling again for their individual tuning of their power levels prior injected into the SOAs. However, the two control signals are now coinciding in time, whereas an additional CW' signal at λ_3 is inserted into the lower branch co-propagating in the respective SOA with the lower cw component. The additional CW' is responsible for controlling independently the induced differential gain saturation at the upper and the lower SOA-MZI arms so as to yield an exact differential phase shift of π rad between the two CW input signal components at the absence of any control pulse, while exhibiting the same gain modulation when a control pulse is injected. Therefore, almost perfect interference conditions are met generating a high quality wavelength converted output signal. Again, interference conditions yield the wavelength converted output signal inverted at the switched port.

As successful WC relies on producing a replica of the original data signal onto the wavelength of the CW input signal, the spectral content of the original signal has to be transferred to the SOA-MZI output without experiencing any frequency dependent

alterations. To this end, the transfer function of an ideal WC device should follow the profile of a low-pass filtering element with a flat frequency response and with its -3dB cut-off frequency denoting the maximum bit-rate that can be supported, as shown in Fig.3. Fig.3 depicts the ideal frequency domain transfer function that should apply to the single SOA-MZI when WC operation is targeted.

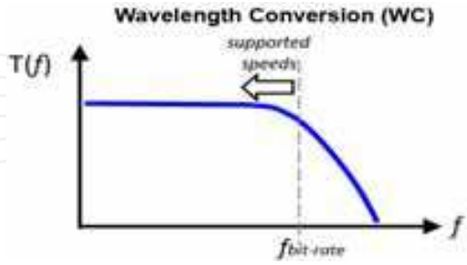

Fig. 3. Ideal frequency domain transfer function for the SOA-MZI based wavelength conversion operation

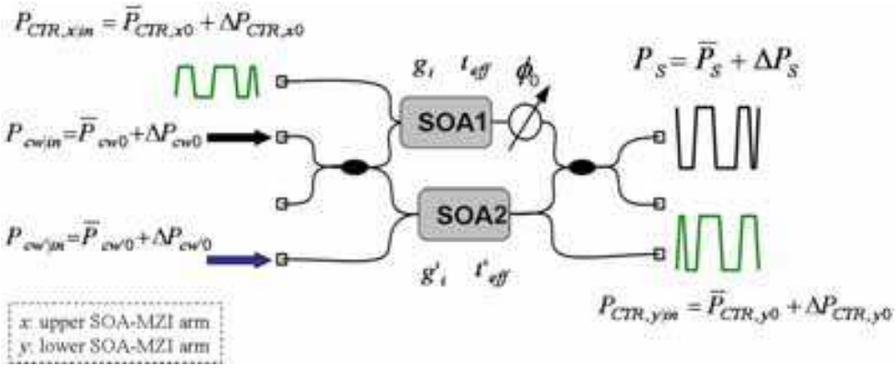

Fig. 4. Generic layout of SOA-MZI all-optical wavelength converter

In order to perform a theoretical frequency domain analysis of the SOA-MZI under wavelength conversion operation, a generic layout of the SOA-MZI AOWC has to be employed that will be capable at expressing all three sub-cases. Fig.4 depicts a generic layout of SOA-MZI AOWC, depicting the input and output signals that may be employed in all schemes. As such, a cw signal with λ_1 wavelength is inserted in the input port of the SOA-MZI while two counter propagating control signals of λ_2 wavelength are considered at the input of upper and lower branches of the SOA-MZI respectively. Finally, an additional cw′ signal of λ_3 wavelength is considered at the input of the lower SOA-MZI branch. Note that each of the possible SOA-MZI AOWC configurations may be retrieved when eliminating the unnecessary inputs. For example, the standard SOA-MZI scheme is retrieved when considering $P_{cw'}=0$ and $P_{CTR,y}=0$, while PUSH-PULL SOA-MZI scheme is retrieved when considering $P_{cw'}=0$. To this end, the derivation of a mathematical expression that describes the frequency response of the SOA-MZI AOWC generic layout will serve in easily extracting the frequency domain transfer function for each of the SOA-MZI schemes, simply by incorporating in the final expression the input signal assumptions described. Finally, one important assumption is that the lower branch control signal is a copy of the upper branch control signal with different power levels and a differential time delay.This indicates that $P_{CTR,y}$ should be expressed as $P_{CTR,y}= mP_{CTR,x} \exp(-j\omega\tau)$.

2.2 Frequency domain analysis theory development

In this section, we theoretically derive an analytical expression for the frequency domain transfer function for the SOA-MZI AOWC generic layout by employing simple approximations for modeling the SOA carrier dynamics based on first order perturbation theory. This will allow to gain qualitative insight in the efficiency of the wavelength conversion functionality versus operational frequency while allowing for the investigation of key device parameters on the wavelength conversion performance such as the material gain and the effective carrier lifetime of the SOAs.

Our approach relies on small-signal analysis and first-order perturbation theory approximations for describing the response of both the SOA devices and the interferometer, following the principles employed in (Davies et al., 1999; Marcenac et al 1997;Nielsen et al 2004). As both the SOA and the MZI configuration are governed by strongly nonlinear coupled equations, small-signal analysis and perturbation theory are employed in order to reduce them into linear expressions so as to enable their subsequent frequency domain treatment towards extracting their transfer function. The employment of first-order perturbation theory tools allows for the description of every time-dependent physical quantity as a sum of a direct current (dc) term and a perturbing term, which in our case is considered to oscillate at a frequency ω. To this end, every time-dependent variable X(t) incorporated in the equations governing the SOA-MZI layout is approximated as

$$X(t)=X_{dc}+\Delta X\cdot e^{j\omega t} \tag{1a}$$

By applying this formalism in a nonlinear equation, separating the dc- from the perturbing-equation terms and neglecting all higher order perturbing terms, two distinct linear equations are obtained: one employing the dc components and one employing all oscillating expressions. This simplifies their solution procedure, leading to linear relationships for the final system's expressions

As shown in Fig. 4, the power of every signal *i* follows the formalism $P_i = \overline{P_i} + \Delta P_i$, where $\overline{P_i}$ represents a steady state term and ΔP_i represents a small perturbation superimposed on it. The SOA-MZI CW input signal employs only a dc power component $\overline{P}_{cw}$ that is split into two equal parts prior entering the SOAs, so that the power expressions of the CW signal components at the x- and y-branch SOA inputs equal:

$$\overline{P}_{cw,x0} = \overline{P}_{cw,y0} = \overline{P}_{cw} / 2$$

The two spatial CW signal components are forced to interfere at the output 3dB coupler of the SOA-MZI after propagating through the x- and y- MZI arms and the respective SOA1 and SOA2 modules. This interference results to an optical power P_S emerging at the S-port of the MZI that is provided by the well-known expression (Pleros et al 2004):

$$P_s = \frac{1}{4}\cdot\left(P_{cw,x} + P_{cw,y} - 2\sqrt{P_{cw,x}\cdot P_{cw,y}}\cdot\cos\left(\phi_0 + \phi_{cw,x} - \phi_{cw,y}\right)\right) \tag{1b}$$

, where $P_{cw,x}$ and $P_{cw,y}$ stand for the power levels and $\phi_{cw,x}$, $\phi_{cw,y}$ denote the respective phase values of the x- and y-branch CW signal constituents when interfering at the MZI output 3dB coupler. By writing the power and phase quantities again as the sum of a dc and a perturbing signal component at frequency ω, i.e.

$$P_{cw,x} = \overline{P}_{cw,x} + \Delta P_{cw,x}\,, \tag{2a}$$

$$P_{cw,y} = \overline{P}_{cw,y} + \Delta P_{cw,y}\,, \tag{2b}$$

$$\phi_{cw,x} = \overline{\phi}_{cw,x} + \Delta\phi_{cw,x}\,, \tag{2c}$$

$$\phi_{cw,y} = \overline{\phi}_{cw,y} + \Delta\phi_{cw,y} \tag{2d}$$

and expanding equation (1) into a first-order Taylor series around $[\Delta P_{cw,x}, \Delta P_{cw,y}, \Delta\phi_{cw,x}, \Delta\phi_{cw,y}]$=[0,0,0,0], the P_S output power can be expressed as:

$$P_s = \frac{1}{4}\cdot\left\{\begin{array}{l}\overline{P}_{cw,x} + \overline{P}_{cw,y} - 2\cdot\sqrt{\overline{P}_{cw,x}\cdot\overline{P}_{cw,y}}\cdot\cos\left(\phi_0 + \overline{\phi}_{cw,x} - \overline{\phi}_{cw,y}\right) + \\ + \left[1 - \dfrac{\overline{P}_{cw,y}}{\sqrt{\overline{P}_{cw,x}\cdot\overline{P}_{cw,y}}}\cdot\cos\left(\phi_0 + \overline{\phi}_{cw,x} - \overline{\phi}_{cw,y}\right)\right]\cdot\Delta P_{cw,x} + \\ + \left[1 - \dfrac{\overline{P}_{cw,x}}{\sqrt{\overline{P}_{cw,x}\cdot\overline{P}_{cw,y}}}\cdot\cos\left(\phi_0 + \overline{\phi}_{cw,x} - \overline{\phi}_{cw,y}\right)\right]\cdot\Delta P_{cw,y} + \\ + 2\cdot\sqrt{\overline{P}_{cw,x}\cdot\overline{P}_{cw,y}}\cdot\sin\left(\phi_0 + \overline{\phi}_{cw,x} - \overline{\phi}_{cw,y}\right)\cdot\left(\Delta\phi_{cw,x} - \Delta\phi_{cw,y}\right)\end{array}\right\} \tag{3}$$

The steady-state term $\overline{P}_s$ and the perturbing term ΔP_s of the switched output power can now be easily identified as:

$$\overline{P}_s = \frac{1}{4}\cdot\left(\overline{P}_{cw,x} + \overline{P}_{cw,y} - 2\cdot\sqrt{\overline{P}_{cw,x}\cdot\overline{P}_{cw,y}}\cdot\cos\left(\phi_0 + \overline{\phi}_{cw,x} - \overline{\phi}_{cw,y}\right)\right) \tag{4}$$

and

$$\Delta P_s = \frac{1}{4}\cdot\left\{\begin{array}{l}\left[1 - \dfrac{\overline{P}_{cw,y}}{\sqrt{\overline{P}_{cw,x}\cdot\overline{P}_{cw,y}}}\cdot\cos\left(\phi_0 + \overline{\phi}_{cw,x} - \overline{\phi}_{cw,y}\right)\right]\cdot\Delta P_{cw,x} + \\ + \left[1 - \dfrac{\overline{P}_{cw,x}}{\sqrt{\overline{P}_{cw,x}\cdot\overline{P}_{cw,y}}}\cdot\cos\left(\phi_0 + \overline{\phi}_{cw,x} - \overline{\phi}_{cw,y}\right)\right]\cdot\Delta P_{cw,y} + \\ + 2\cdot\sqrt{\overline{P}_{cw,x}\cdot\overline{P}_{cw,y}}\cdot\sin\left(\phi_0 + \overline{\phi}_{cw,x} - \overline{\phi}_{cw,y}\right)\cdot\left(\Delta\phi_{cw,x} - \Delta\phi_{cw,y}\right)\end{array}\right\} \tag{5}$$

The theoretical analysis carried out so far applies to any type of MZI interferometers even when nonlinear media different than SOAs are employed in the MZI arms. Moreover, the wavelength conversion efficiency η_{WC} of the SOA-MZI is obtained by the ratio of the acquired over the initial perturbation, given in equation (6) below.

$$\eta_{WC} = \frac{\Delta P_s}{\Delta P_{CTR,x}} \tag{6}$$

Our goal is to express the perturbing component of the output ΔP_s as a linear function of the perturbing component of the input $\Delta P_{CTR.x}$, so as to obtain an expression of the wavelength conversion efficiency η_{WC} that is independent from the input signal. However, the exact solutions of (4) and (5) can only be derived if the nonlinear medium characteristics and their impact onto the propagating signal are taken into consideration in order to allow for the analytic expressions of both the steady-state and the perturbing power and phase terms at the two x- and y- branch CW signal components. This implies that analytic power and phase expressions in the case of the SOA-MZI can be only obtained by taking into account the interaction of the propagating beams with the respective SOA1 and SOA2 devices.
The SOA carrier dynamics are described by a rate equation model that relates the power (7) and the phase (8) of every input signal i with the carrier density N,

$$\frac{\partial P_i}{\partial z} = \left[\Gamma \cdot \alpha_i \cdot \left(N - N_{t,i}\right) - a_{\text{int}}\right] \cdot P_i \tag{7}$$

$$\frac{\partial \phi_i}{\partial z} = -\frac{1}{2} \cdot \alpha_f \cdot \Gamma \cdot \alpha_i \cdot N \tag{8}$$

where Γ is the confinement factor, a_i is the gain parameter at wavelength i, N is the carrier density and $N_{t,i}$ is the carrier density at transparency, a_f is the linewidth enhancement factor and a_{int} is the internal waveguide loss of the semiconductor. Following the same approach as we did for describing the optical signal power, both the phase information of the signals and the carrier density of the SOA device are expressed as the sum of a steady state term and a small varying term, respectively. Separating the steady state from the perturbation terms, in equations (7) and (8), generates a new set of equations (9)-(12) describing the evolution of the steady state terms $\bar{P}_i$ and $\bar{\phi}_i$ and the evolution of the perturbation terms ΔP_i and $\Delta\phi_i$ for the power and phase, along the propagation axis z.

$$\frac{\partial \bar{P}_i}{\partial z} = \left[\Gamma \cdot \alpha_i \cdot \left(\bar{N} - N_{t,i}\right) - a_{\text{int}}\right] \cdot \bar{P}_i \tag{9}$$

$$\frac{\partial \Delta P_i}{\partial z} = \left[\Gamma \cdot \alpha_i \cdot \left(\bar{N} - N_{t,i}\right) - a_{\text{int}}\right] \cdot \Delta P_i + \Gamma \cdot \alpha_i \cdot \Delta n \cdot \bar{P}_i \tag{10}$$

$$\frac{\partial \bar{\phi}_i}{\partial z} = -\frac{1}{2} \cdot \alpha_f \cdot \Gamma \cdot \alpha_i \cdot \left(\bar{N} - N_{t,i}\right) \tag{11}$$

$$\frac{\partial \Delta\phi_i}{\partial z} = -\frac{\alpha_f}{2} \cdot \Gamma \cdot \alpha_i \cdot \Delta n \tag{12}$$

Δn describes the SOA carrier density change as given in (Davies et al 1999)

$$\Delta n = \frac{-\sum_i \left(N - N_{t,i}\right) \cdot \frac{\Delta P_i}{E_{sat,i}}}{1/\tau_c + \sum_i 1/\tau_{s,i} + j \cdot \omega} \tag{13}$$

where $E_{sat,i}$ is the saturation energy of the SOA at wavelength λ_i and ω is the cyclic frequency. The effective carrier lifetime of the SOA denoted by t_{eff} is given by $1/t_{eff} = 1/\tau_c + \sum_i 1/\tau_{s,i}$ where, τ_c is the carrier lifetime, $\tau_{s,i}$ is the contribution of the signal i to the effective carrier lifetime and $\tau_{s,i} = E_{sat,i}/\overline{P}_i$ is the stimulated carrier recombination time.

Analytical solution of equations (9)-(12) yields the power and phase information of the signals at the output of every SOA-MZI branch. Throughout the analysis, it has been assumed that the input perturbation imposed by the control signals $\Delta P_{CTR,x0}$ and $\Delta P_{CTR,y0}$ is responsible for modulating the carrier density of the SOAs and that the input continuous wave signals cw and cw′ have no initial perturbation (i.e. $\Delta P_{cw0} = \Delta P_{cw'0} = 0$). It has been further assumed that, the input cw components traveling the upper and lower SOA-MZI branches are responsible for driving the SOAs into deep saturation and dominate their carrier dynamics (i.e. $\overline{P}_{CTR,x0} = \overline{P}_{CTR,y0} = 0$).

At the upper SOA-MZI branch of the SOA-MZI the $CTR_{,x}$ signal imposes a perturbation on the carrier density of the upper SOA described by equation (14),

$$\Delta n = \frac{-\left(\overline{N} - N_{t,cw,x}\right)\cdot\frac{\Delta P_{cw,x}}{E_{sat}} - \left(\overline{N} - N_{t,CTR,x}\right)\cdot\frac{\Delta P_{CTR,x}}{E_{sat}}}{1/t_{eff} + j\cdot\omega} \tag{14}$$

where the effective carrier lifetime of the upper SOA is given by $1/t_{eff} = 1/\tau_c + 1/\tau_{s,cw,x}$ assuming that the contribution of the control signal to the effective carrier lifetime is zero. The power of the upper cw component is obtained solving equations (9),(10) and its phase is obtained solving equations (11),(12) using (14). Therefore, for the steady state terms and the perturbation terms of the power and phase we get,

$$\overline{P}_{cw,x} = \overline{P}_{cw,x0}\cdot\exp\left[\left(g - a_{\text{int}}\right)\cdot z\right] = \frac{\overline{P}_{cw,0}}{2}\cdot\exp\left[\left(g - a_{\text{int}}\right)\cdot z\right] \tag{15}$$

$$\Delta P_{cw,x} = \Delta P_{CTR,x}\cdot\left[\exp\left(\frac{-g\cdot z}{\tau_{s,cw}\cdot\left(1/t_{eff} + j\cdot\omega\right)}\right) - 1\right] \tag{16}$$

$$\overline{\phi}_{cw,x} = -\frac{\alpha_f}{2}\cdot g\cdot z \tag{17}$$

$$\Delta\phi_{cw,x}(z) = -\frac{\alpha_f}{2}\cdot\frac{\Delta P_{CTR,x}}{\left(g - \alpha_{\text{int}}\right) + \frac{(-g)}{\tau_{s,cw}\cdot\left(1/t_{eff} + j\cdot\omega\right)}}\cdot\frac{(-g)}{E_{sat}\cdot\left(1/t_{eff} + j\cdot\omega\right)}\cdot\exp\left[\frac{-g\cdot z}{\tau_{s,cw}\cdot\left(1/t_{eff} + j\cdot\omega\right)}\right] \tag{18}$$

where, $P_{cw,0}$ is the power of the cw signal in the input of the interferometer (Fig.4), g is the modal gain given by $g_i = \Gamma\cdot\alpha_i\cdot\left(N - N_{t,i}\right)$ (Davies et al 1999), where i is denoting the signal wavelength.

In the same way, the optical power of the CTR_x signal at the output of the SOA is obtained by solving (10), taking into account that $\overline{P}_{CTR,x0} = 0$.

$$\Delta P_{CTR,x} = \Delta P_{CTR,x0} \cdot \exp\left[\left(g - a_{\text{int}}\right) \cdot z\right] \tag{19}$$

where $\Delta P_{CTR,x0}$ is the initial perturbation imposed on the CTR_x signal.
At the lower SOA-MZI branch, the additional cw' signal employed is responsible for driving the lower SOA device into a slightly different saturation level than the upper SOA and thus the respective gain parameters are no longer equal (i.e. $g' \neq g$). Furthermore, the SOA dimensions are assumed to be infinitely small and the direction of propagation is not taken into account in this model. Finally, the effective carrier lifetime of the lower SOA device comprises also by the additional contribution of the CW' signal ($1/t'_{eff} = 1/\tau_c + 1/\tau_{s,cw,y} + 1/\tau_{s,cw'}$). At the lower SOA-MZI branch, the CW' signal is additionally contributing to the carrier density change of the lower SOA, now given by equation (20).

$$\Delta n' = \frac{-\left(\overline{N}_0 - N_{t,cw,y}\right) \cdot \frac{\Delta P_{cw,y}}{E_{sat}} - \left(\overline{N}_0 - N_{t,cw',y}\right) \cdot \frac{\Delta P_{cw',y}}{E_{sat}} - \left(\overline{N}_0 - N_{t,CTR,y}\right) \cdot \frac{\Delta P_{CTR,y}}{E_{sat}}}{1/t'_{eff} + j \cdot \omega} \tag{20}$$

The steady state power and phase evolution of the $CW_{,y}$ component are given by equations (21) and (22).

$$\overline{P}_{cw,y} = \overline{P}_{cw,y0} \cdot \exp\left[\left(g' - a_{\text{int}}\right) \cdot z\right] = \frac{\overline{P}_{cw,0}}{2} \cdot \exp\left[\left(g' - a_{\text{int}}\right) \cdot z\right] \tag{21}$$

$$\overline{P}_{cw,'y} = \overline{P}_{cw',y0} \cdot \exp\left[\left(g' - a_{\text{int}}\right) \cdot z\right]$$

$$\overline{\phi}_{cw,y} = -\frac{\alpha_f}{2} \cdot g' \cdot z \tag{22}$$

$$\overline{\phi}_{cw',y} = -\frac{\alpha_f}{2} \cdot g' \cdot z$$

The respective power perturbation of the $CW_{,y}$ signal is described by equation (23), taking into account equation (24), and it is derived following the same analysis.

$$\Delta P_{cw',y} = \frac{\Delta P_{CTR,y} \cdot \overline{P}_{cw',y}}{\overline{P}_{cw,y} + \overline{P}_{cw',y}} \cdot \left\{ \exp\left[\frac{-g' \cdot z \cdot \left(\overline{P}_{cw,y} + \overline{P}_{cw',y}\right)}{E_{sat} \cdot \left(1/t'_{eff} + j \cdot \omega\right)} \right] - 1 \right\} \tag{23}$$

$$\begin{aligned} \Delta P_{cw,y} &= \Delta P_{CTR,y} \cdot \left\{ \exp\left[\frac{-g' \cdot z \cdot \left(\overline{P}_{cw,y} + \overline{P}_{cw',y}\right)}{E_{sat} \cdot \left(1/t'_{eff} + j \cdot \omega\right)} \right] - 1 \right\} - \Delta P_{cw',y} \rightarrow \\ \Delta P_{cw,y} &= \Delta P_{CTR,y} \cdot \left(\exp\left[\frac{-g' \cdot z \cdot \left(\overline{P}_{cw,y} + \overline{P}_{cw',y}\right)}{E_{sat} \cdot \left(1/t'_{eff} + j \cdot \omega\right)} \right] - 1 \right) \left(1 - \frac{\overline{P}_{cw',y}}{\left(\overline{P}_{cw,y} + \overline{P}_{cw',y}\right)} \right) \end{aligned} \tag{24}$$

The spatial evolution of the frequency domain phase variation of the $CW_{,y}$ signal is given

$$\Delta\phi_{cw,y}(z) = -\frac{\alpha_f}{2}\cdot\frac{\Delta P_{CTR,y}}{\left(g'-\alpha_{\text{int}}\right)+\dfrac{\left(-g'\right)\cdot\left(\overline{P}_{cw,y}+\overline{P}_{cw',y}\right)}{E_{sat}\cdot\left(1/t_{eff}^{'}+j\cdot\omega\right)}}\cdot\frac{\left(-g'\right)}{E_{sat}\cdot\left(1/t_{eff}^{'}+j\cdot\omega\right)}\cdot\exp\left[\frac{-g'\cdot z\cdot\left(\overline{P}_{cw,y}+\overline{P}_{cw',y}\right)}{E_{sat}\cdot\left(1/t_{eff}^{'}+j\cdot\omega\right)}\right] \quad (25)$$

To this end, the wavelength conversion efficiency of the differentially biased SOA-MZI scheme can be analytically derived by substituting (15)-(19) and (21)-(25) in equations (5) and (6).

$$\eta_{WC}=\frac{1}{4}\cdot$$
$$\left|\begin{array}{l}\left(1-\sqrt{\dfrac{\exp(g'-a_{\text{int}})z}{\exp(g-a_{\text{int}})z}}\cos(\phi_o-\frac{a_f}{2}(g'-g))\right)\left(\exp\left(\dfrac{-g\cdot z}{\tau_{s,cw}\cdot\left(1/t_{eff}+j\cdot\omega\right)}\right)-1\right)+\\ \left(m\exp(j\omega T)\left(1-\sqrt{\dfrac{\exp(g-a_{\text{int}})z}{\exp(g'-a_{\text{int}})z}}\cos(\phi_o-\frac{a_f}{2}(g'-g))\right)\cdot\left(\exp\left[\dfrac{-g'\cdot z\cdot\left(\overline{P}_{cw,y}+\overline{P}_{cw',y}\right)}{E_{sat}\cdot\left(1/t_{eff}^{'}+j\cdot\omega\right)}\right]-1\right)\left(1-\dfrac{\overline{P}_{cw',y}}{\left(\overline{P}_{cw,y}+\overline{P}_{cw',y}\right)}\right)\right)-\\ \dfrac{a_f\cdot(-g)}{\tau_{S,CW}}\sqrt{\dfrac{\exp(g'-a_{\text{int}})z}{\exp(g-a_{\text{int}})z}}\sin(\phi_0-\frac{a_f}{2}(g'-g))\cdot\\ \left(\dfrac{\exp\left[\dfrac{-g\cdot z}{\tau_{s,cw}\cdot\left(1/t_{eff}+j\cdot\omega\right)}\right]}{\left(1/t_{eff}+j\cdot\omega\right)\left(\left(g-\alpha_{\text{int}}\right)+\dfrac{(-g)}{\tau_{s,cw}\cdot\left(1/t_{eff}+j\cdot\omega\right)}\right)}-\dfrac{m\exp(j\omega T)\cdot\exp\left[\dfrac{-g'\cdot z\cdot\left(\overline{P}_{cw,y}+\overline{P}_{cw',y}\right)}{E_{sat}\cdot\left(1/t_{eff}^{'}+j\cdot\omega\right)}\right]}{\left(\left(g'-\alpha_{\text{int}}\right)+\dfrac{\left(-g'\right)\cdot\left(\overline{P}_{cw,y}+\overline{P}_{cw',y}\right)}{E_{sat}\cdot\left(1/t_{eff}^{'}+j\cdot\omega\right)}\right)\left(1/t_{eff}^{'}+j\cdot\omega\right)}\right)\end{array}\right| \quad (26)$$

3. SOA-MZI AOWC frequency domain transfer function analysis

3.1 Standard SOA-based MZI scheme

Standard SOA-based MZI scheme is the simplest configuration for performing wavelength conversion. This scheme can be modeled by equation (26) if we consider that at the lower SOA-MZI arm there is no input perturbation, i..e $P_{CTR,y}$ = 0 and $\Delta P_{CTR,y}$ = 0. This is represented in (26) by setting m=0. Moreover, there is no second CW signal entering the lower SOA-MZI arm, leading to $P_{CW',y}$=0. Thus, the modal gain g' of the lower SOA equals g since the upper and lower SOAs are driven into the same saturation level (i.e. $\overline{P}_{cw,x0}=\overline{P}_{cw,y0}=\overline{P}_{cw0}/2$). By setting in (26) *m=0, g=g'* and *$P_{CW',y}$=0* we derive the analytical expression of the wavelength conversion efficiency for the standard SOA-MZI scheme given by

$$\eta_{STD}(z,\omega)=\frac{1}{4}\cdot\left|\left(1-\cos(\phi_0)\right)\cdot\left\{\exp\left[\frac{-g\cdot z}{\tau_{s,cw}\cdot\left(1/t_{eff}+j\cdot\omega\right)}\right]-1\right\}-\frac{\alpha_f\cdot\sin(\phi_0)(-g)\exp\left[\dfrac{-g\cdot z}{\tau_{s,cw}\cdot\left(1/t_{eff}+j\cdot\omega\right)}\right]}{\tau_{s,cw}\cdot\left(1/t_{eff}+j\cdot\omega\right)\left(\left(g-\alpha_{\text{int}}\right)+\dfrac{(-g)}{\tau_{s,cw}\cdot\left(1/t_{eff}+j\cdot\omega\right)}\right)}\right| \quad (27)$$

Equation (27) provides an analytical expression for the frequency-domain transfer function of the SOA-MZI configuration. Fig. 5 depicts the respective normalized S-port conversion efficiency versus frequency for various values of the gz factor assuming that t_{eff} is 50psec, z=1mm and τ_c=200psec. As shown in Fig.5(a), three different operational regions with respect to the total gain gz can be identified for the MZI response. For small gz values like 1 and 3, the MZI frequency response resembles that of a low-pass filtering element with a rather low 3-dB bandwidth that increases with gz. When gz continues to increase reaching gz=5, the MZI response extends to higher frequencies but exhibits a resonance peak around 10GHz forming a transfer function shape that is more similar to that of a band-pass filter centered around this resonance, as shown experimentally in (Yan et al 2009). As gz exceeds the value of 5 approaching higher total gain values, this resonance peak continues to exist

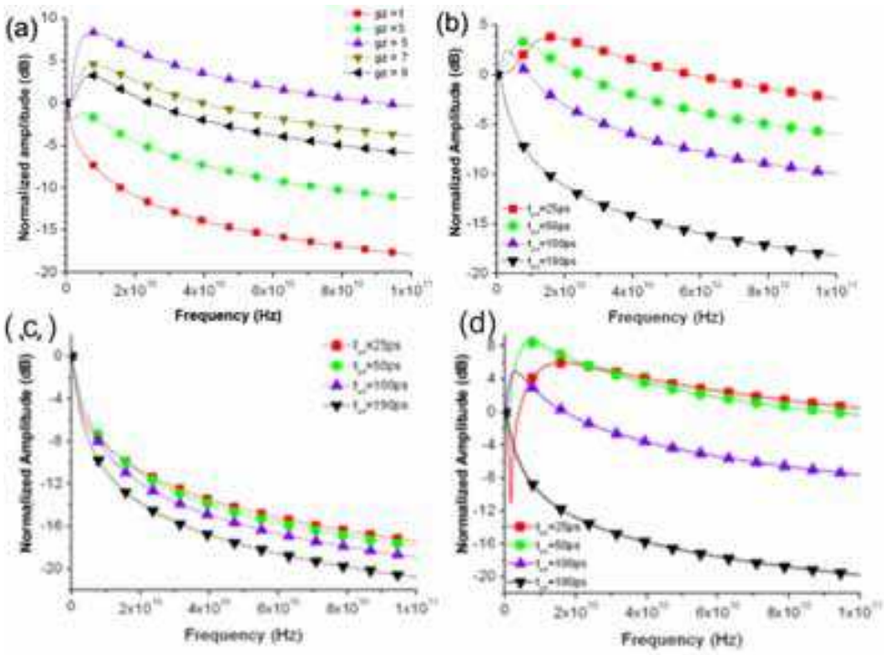

Fig. 5. a) The SOA-MZI frequency response for different total gain values and for an effective SOA gain recovery time of 50psec, (b,c,d) SOA-MZI response with high SOA gain for four different t_{eff} values (25ps,50ps, 100ps, 190ps) (b) gz=9, (c) gz=1, (d) gz=5.

becoming, however, significantly weaker as gz increases. This indicates that the MZI response tends to develop a smoother frequency dependence for frequencies up to 25 GHz with spectral amplitude deviations residing within a 3dB limit. The existence of a resonance peak with varying amplitude depending on the SOA gain conditions has been presented experimentally in (Cao et al 2002).

Fig. 5(b) depicts the SOA-MZI response when high SOA gain operation is utilized, again for the four different t_{eff} values. A low recovery time of 190psec yields just a low-pass filtering characteristic curve with small bandwidth values, but when t_{eff} decreases below 100psec the bandwidth is significantly enhanced extending beyond 40GHz for t_{eff}=25psec. At the same time, the MZI response continues to exhibit a resonance peak around a certain frequency that shifts to higher values for decreasing t_{eff}, however its effect is significantly weaker than in the case of moderate SOA gain levels, having an amplitude that is only 3dB higher

compared to the amplitudes of the lower frequency components. This suggests that increased gain values yield a smoother frequency dependence with higher supporting bandwidths, indicating this region as the operational regime in WC applications.
Optimization of the SOA-MZI operational parameters with respect to each separate application can be achieved by proper control of the SOA gain recovery dynamics. The dependence of the SOA-MZI frequency response on the effective SOA carrier recovery time for all three different operational regimes is depicted in Fig.5 (a). Fig. 5(c) shows the transfer function for a gz=1 value and for four different t_{eff} values ranging between 25psec and 190psec. A typical low-pass filter transfer function can be observed with a 3-dB bandwidth being always below 1GHz and decreasing as t_{eff} increases.
Figure 5(d) illustrates the four graphs of the SOA-MZI response obtained for the respective t_{eff} values of 25, 50, 100 and 190 psec and for a SOA gain level of gz=5. In the case of 190 psec recovery times the transfer function is again a low-pass filtering curve, however its shape changes dramatically when t_{eff} values lower than 100psec are used: the MZI response exhibits a resonance peak around a certain frequency that shifts to higher frequency values as t_{eff} is decreasing. This resonance implies that the SOA-MZI circuit starts to behave like a band-pass filtering device suppressing the power of the frequency components lying around the central resonance. This effect is even more pronounced when t_{eff}=25psec, where the spectral content between 0 and 8 GHz is suppressed by more than 3dB compared to the approximately 12GHz resonant frequency, reaching in some spectral areas around the 3GHz region also suppression values up to 15dB.

3.2 Differential time delay ("Push-Pull") configuration

The differential delay configuration relies on the principle that the output modulated signal is the portion of the initial CW that falls within the switching window induced by the non-perfect overlapping of the two control signals. Moreover, the broadness of the switching window is controlled by differential time delay imposed between the two control signals. To this end, the switching window can be set to be very thin, dramatically increasing the capacity for very high frequencies wavelength conversion operations at the expense of reduced noise figure. However, numerous experimental setups have demonstrated successful operation for high bit rate WC employing the differential delay scheme, including 40 Gb/s wavelength conversion (Wolfson et al. 2000, Leuthold et al. 2001, Nakamura 2001).
Frequency domain analysis allows for a thorough investigation of the WC operation in order to reveal its limitations and suggest a systematic optimization procedure. The wavelength conversion efficiency for differential time delay scheme is analytically described by equation (26) by considering the modal gains of the upper (g) and lower (g') SOAs equal (g=g'), as the absence of a second CW signal entering the lower SOA-MZI branch ($P_{CW,y=0}$) allows SOA carrier density modulation imposed by the CTRy data signal to be copied to the amplitude and phase of the lower cw component. Hence, equal power level of control signals at the upper and lower SOA-MZI arms induce the same gain saturation. Moreover, initial perturbations imposed by the control signals are related through the parameter m taking values within the range (0,1]. Differential time delay between the two SOA-MZI branches is expressed through the perturbation $\Delta P_{CTR,y}$ in the lower branch of the interferometer, as the time delay with respect to the perturbation $\Delta P_{CTR,x}$ of the upper branch is expressed as $\Delta P_{CTR,y0} = m \cdot \Delta P_{CTR,x0} \exp\left[j\omega \Delta T \right]$, where ΔT is the differential time delay.

Substituting these considerations in (26) leads in the following expression for the wavelength conversion efficiency of the differential delay scheme :

$$\eta_{DELAY}(z,\omega)=\frac{1}{4}\left|\begin{array}{l}\left(m\cdot\exp[j\omega\Delta T]+1\right)(1-\cos(\varphi_0)\cdot\left\{\exp\left[\dfrac{-g\cdot z}{\tau_{s,cw}\cdot\left(1/t_{eff}+j\cdot\omega\right)}\right]-1\right\}- \\ a_f\sin(\varphi_0)\cdot\left(1-m\cdot\exp[j\omega\Delta T]\right)\cdot\dfrac{(-g)\exp\left[\dfrac{-g\cdot z}{\tau_{s,cw}\cdot\left(1/t_{eff}+j\cdot\omega\right)}\right]}{\tau_{s,cw}\cdot\left(1/t_{eff}+j\cdot\omega\right)\left(\left(g-\alpha_{\text{int}}\right)+\dfrac{(-g)}{\tau_{s,cw}\cdot\left(1/t_{eff}+j\cdot\omega\right)}\right)}\end{array}\right| \quad (28)$$

Based on (28), the first row of graphs in Figure 6 (a,b,c) depict the normalized frequency response for the differentially biased SOA-MZI AOWC for different time delay values, namely Δτ=1ps (a), Δτ=20ps (a) and Δτ=50ps (c). The t_{eff} for all graphs is 100 ps while the five lines on each graph correspond to different values of modal gain (gz=1,3,5,7,9). Finally, for Fig. 6 (a,b,c) the frequency response is optimized versus the power ratio m by means of flattening the transfer function. The graphs clearly show that the differential delay scheme can significantly broaden the dyanmic range of wavelength conversion operation to very high frequencies even when employing slow SOAs (t_{eff} = 100 ps), as the flat area of the frequency response exceeds the 10 GHz in all graphs. Especially in Fig.6(a) that corresponds to Δτ=1ps, an effective bandwidth of at least 100 GHz is revealed for successful wavelength conversion. In fact, the cut-off frequency is inversely proportional to the differential time delay Δτ employed, as this is limited by periodic zero points of the transfer function at frequency values equal to 1/Δτ.

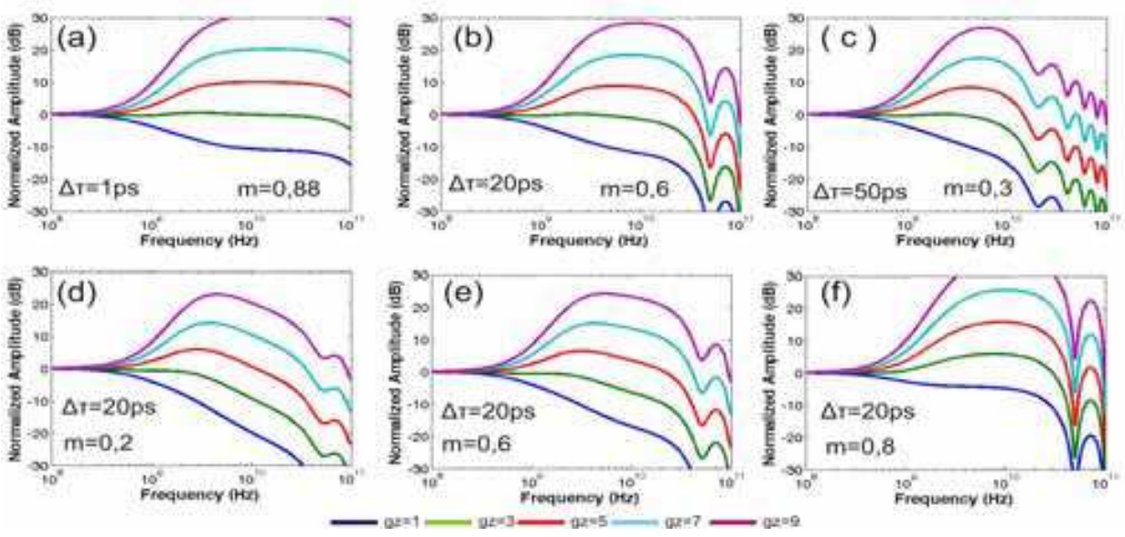

Fig. 6. (a,b,c) normalized frequency response for the differentially biased SOA-MZI AOWC for different time delay values (1ps,20ps,50ps),(d,e,f) normalized frequency response for Δτ=20ps and different contorl signal power ratio values.

Frequency response optimization of the differential time delay scheme for a given Δτ is strongly dependent on the parameters gz (gain) and m (control signals power ratio). For the gain parameter, lower values of gain are more tolerant to control signals power ratio variations, meaning that they allow a flat frequency response for a wider range of m and for that reason they are preferable. On the other hand, control signals power ratio m is critical in achieving a flat frequency response, as shown by the graphs in Fig. 6(d,e,b,f).

These graphs depict the frequency response for a differential time delay Δτ=20ps, for values of m equal to m=0,2, m=0,4, m=0,6 and m=0,8 respectively. Higher values of m tend to lift the higher frequencies response while the part until 1GHz remains unaffected. The analysis also shows that higher differential time dealy values require smaller values of m in order to achieve optimum performance. This is evident if we consider the physical mechanism of the differential time delay scheme: as the lower control signal is time delayed compared to the upper control signal, its power has to decrease in order to fit the exponential recovery of the SOA and cancel it out.

3.3 Differentially biased SOA-based MZI scheme

The additional CW′ signal employed in the differentially biased SOA-MZI scheme is responsible for driving the lower SOA device into a slightly different saturation level than upper SOA and thus the respective gain parameters are no longer equal (i.e. $g' \neq g$). Moreover, the power levels of the continuous wave signals are such that a differential phase shift of π rad between the two SOA-MZI branches is achieved, yielding $g' = g - 2\pi / \alpha_f$. The carrier dynamics of the upper SOA device is dominated by the same effective carrier lifetime with the one given for the standard and bidirectional schemes ($1/t_{eff} = 1/\tau_c + 1/\tau_{s,cw,x}$), whereas the effective carrier lifetime of the lower SOA device comprises also by the additional contribution of the cw' signal ($1/t'_{eff} = 1/\tau_c + 1/\tau_{s,cw,y} + 1/\tau_{s,cw'}$). The wavelength conversion efficiency of the differentially biased SOA-MZI scheme is expressed as

$$\eta_{DIF} = \frac{1}{4}\cdot \left| \begin{array}{l} \left(1 - \sqrt{\frac{\exp(g'-a_{\text{int}})z}{\exp(g-a_{\text{int}})z}}\cos(\varphi_o - \frac{a_f}{2}(g'-g))\right)\left(\exp\left(\frac{-g\cdot z}{\tau_{s,cw}\cdot\left(1/t_{eff}+j\cdot\omega\right)}\right)-1\right)+ \\ \left(m\left(1 - \sqrt{\frac{\exp(g-a_{\text{int}})z}{\exp(g'-a_{\text{int}})z}}\cos(\varphi_o - \frac{a_f}{2}(g'-g))\right)\cdot\left(\exp\left[\frac{-g'\cdot z\cdot\left(\overline{P}_{cw,y}+\overline{P}_{cw',y}\right)}{E_{sat}\cdot\left(1/t'_{eff}+j\cdot\omega\right)}\right]-1\right)\left(1-\frac{\overline{P}_{cw',y}}{\left(\overline{P}_{cw,y}+\overline{P}_{cw',y}\right)}\right)\right)- \\ \frac{a_f\cdot(-g)}{\tau_{S,CW}}\sqrt{\frac{\exp(g'-a_{\text{int}})z}{\exp(g-a_{\text{int}})z}}\sin(\varphi_0 - \frac{a_f}{2}(g'-g))\cdot \\ \left(\frac{\exp\left[\frac{-g\cdot z}{\tau_{s,cw}\cdot\left(1/t_{eff}+j\cdot\omega\right)}\right]}{\left(1/t_{eff}+j\cdot\omega\right)\left(\left(g-\alpha_{\text{int}}\right)+\frac{(-g)}{\tau_{s,cw}\cdot\left(1/t_{eff}+j\cdot\omega\right)}\right)}-\frac{m\cdot\exp\left[\frac{-g'\cdot z\cdot\left(\overline{P}_{cw,y}+\overline{P}_{cw',y}\right)}{E_{sat}\cdot\left(1/t'_{eff}+j\cdot\omega\right)}\right]}{\left(\left(g'-\alpha_{\text{int}}\right)+\frac{(-g')\cdot\left(\overline{P}_{cw,y}+\overline{P}_{cw',y}\right)}{E_{sat}\cdot\left(1/t'_{eff}+j\cdot\omega\right)}\right)\left(1/t'_{eff}+j\cdot\omega\right)}\right) \end{array} \right| \quad (29)$$

The normalized frequency response for the differentially biased SOA-MZI AOWC, depicted in Fig. 7(a) for t_{eff} 25 ps is flat at low frequencies and starts to decrease above 20 GHz, exhibiting low-pass filter characteristics and resembling the ideal transfer function for WC as described in Fig. 3. In this case, the 3 dB cut-off frequency indicating the speed capabilities for efficient wavelength conversion operation, reaches several tenths of GHz when the gain value increases up to 9. For longer effective carrier lifetime (t_{eff} = 100 ps), the frequency response curves for the differentially biased SOA-MZI schemes shifts towards lower frequencies, limiting the available wavelength conversion bandwidth below 2-3 GHz, as illustrated in Fig. 7(b).

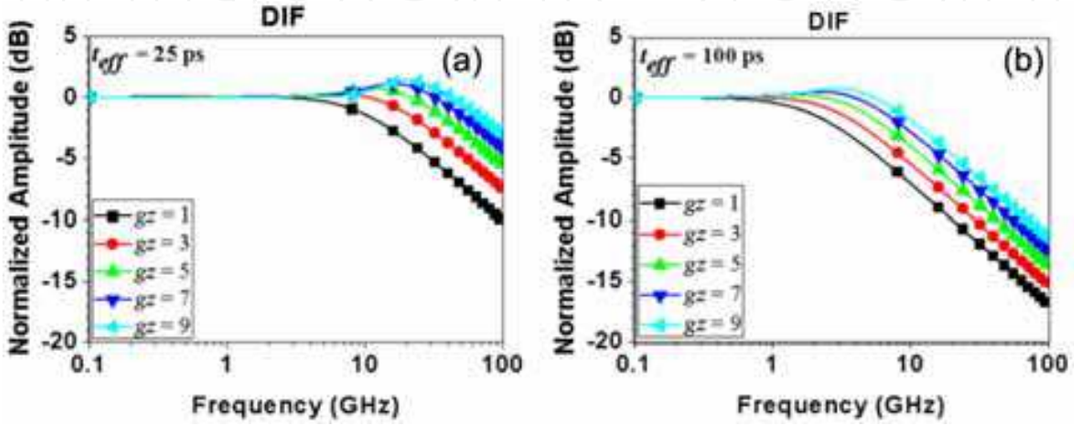

Fig. 7. Normalized frequency response for the differentially biased SOA-MZI AOWC, (a) for t_{eff} 25 ps (b) for t_{eff} 100 ps

3.4 Origin of the frequency domain behavior: XPM/XGM

In order to gain insight into the physical mechanisms dominating the carrier dynamics of the SOA-MZI AOWC and to unveil the key role of the $\Delta P_{CTR,y}$ and *cw*' signals, we treat the generic frequency domain transfer function given by equation (29) as a sum of two terms and we investigate their individual contributions to the overall AOWC frequency response. The first term is governed by the amplitude modulation (*AM*) $\Delta P_{cw,x}$ and $\Delta P_{cw,y}$ acquired by the two interfering cw components at the output of the upper and lower SOA-MZI branch whilst, the second term is governed by the difference of their acquired phase modulation (*PM*) $\left(\Delta\phi_{cw,x} - \Delta\phi_{cw,y}\right)$, respectively, given by equations (30) and (31).

$$\eta_{AM} = \frac{1}{4 \cdot \Delta P_{CTR,x}} \cdot \left\{ A(z,\omega) \cdot \Delta P_{cw,x} + B(z,\omega) \cdot \Delta P_{cw,y} \right\} \tag{30}$$

$$\eta_{PM} = \frac{1}{4 \cdot \Delta P_{CTR,x}} \cdot C(z,\omega) \cdot \left(\Delta\phi_{cw,x} - \Delta\phi_{cw,y} \right) \tag{31}$$

Fig. 8(a) illustrates the individual frequency domain responses of η_{AM} and η_{PM} on the left and middle graphs, and the normalized with respect to the total SOA-MZI AOWC transfer function, for three different values of *m* and three different states of the induced differential phase shift Δφ between the two SOA-MZI branches. On the right, the normalized total

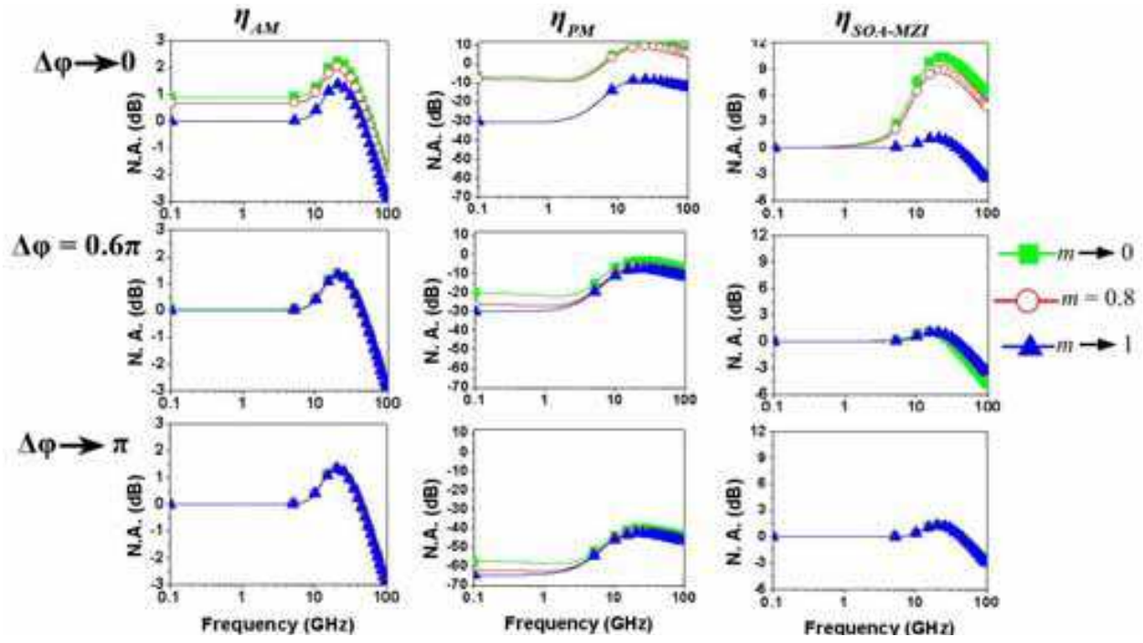

Fig. 8. Normalized amplitude (N.A.) frequency response of η_{AM} (left) and η_{PM} (middle) with respect to the total transfer function (right) for various values of m and the differential phase shift Δφ. Results shown for SOA effective carrier lifetime 25 ps and gain 9.

frequency response is illustrated to allow for direct comparison. When both Δφ and m are close to 0, the total transfer function resembles a bandpass frequency response that is mainly attributed to the contribution of the η_{PM} term, corresponding to the standard SOA-MZI AOWC operation. At the same time, increasing m, which is equivalent to introducing the control signal $\Delta P_{CTR,y}$ at the lower SOA-MZI branch, suppresses η_{PM} by 20 dB and yields an almost flat total response dominated by the η_{AM} term. In the case that the additional CW' signal is introduced yielding a differential phase shift of 0.6π, the η_{PM} contribution is still suppressed for all m values, and the total response also follows the characteristic shape of η_{AM}. A strong control signal (m→1) at the lower SOA-MZI branch is required in order to shift the total transfer function towards higher frequencies and thus to increase the AOWC operation speed. Finally, when Δφ is very close to π rad corresponding to the differentially biased SOA-MZI AOWC scheme, the SOA-MZI is fully balanced for all m values yielding optimum interference of the two cw components.

3.5 Theoretical assessment of SOA-MZI-based System Applications: PED and CR

The theoretical analysis presented in this chapter may expand in order to create a theoretical tool that is able to be applied in the various multi-functional applications whose architecture is based on SOA-MZIs. To this end, this section presents two examples that will assess a theoretical performance analysis in critical SOA-MZI based applications, such as the FPF-assisted SOA-MZI circuit in both Packet envelope detection and and Clock Recovery operations. Fig.9 illustrates the SOA-MZI configurations when performing in two different signal processing functionalities: Fig.9(a) and 9(b) depict a SOA-MZI assisted by a FPF and operating as PED (Stampoulidis et al 2007) and as CR circuit (Kanellos et al 2007),

respectively. In both system architectures, the SOA-MZI comprises two SOAs, with SOA1 located at the upper and SOA2 at the lower MZI arm, and is powered by a CW optical beam used as the input signal.

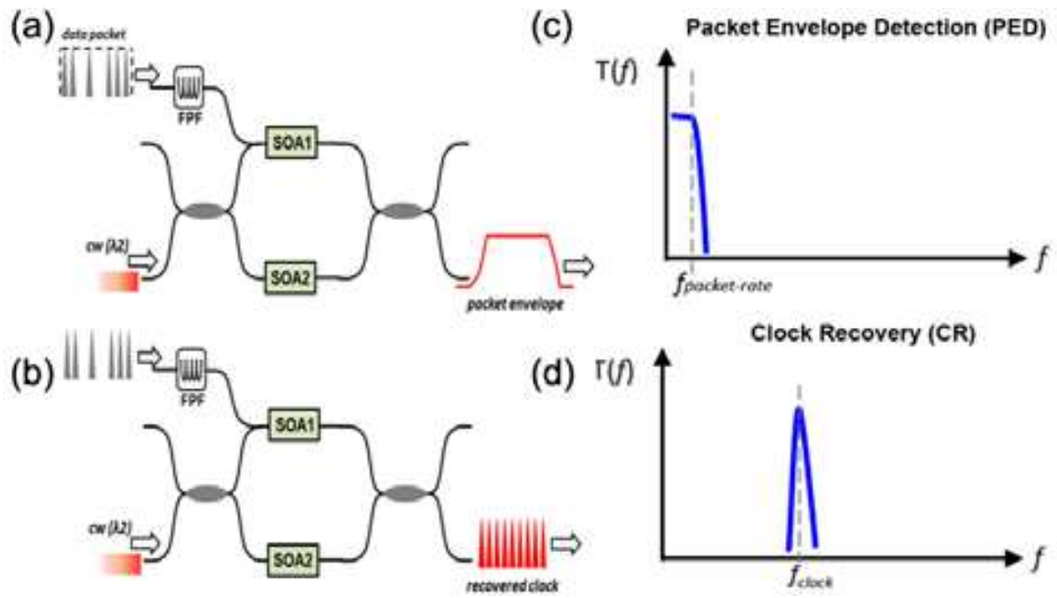

Fig. 9. (a,b) PED and CR setup employing a AOWC MZI and FPF filter, (c,d) ideal transfer functions for PED and CR operation.

When operating as PED or CR circuit, shown in Fig. 9(a) and 9(b), respectively, the optical data signal travels through a low-Finesse FPF prior entering SOA1 as the CTR signal, with the FPF having a Free-Spectral Range (FSR) equal to the data line-rate. As a result, the light signal obtained at the FPF output resembles a strongly amplitude modulated clock pulse signal that has a slightly enhanced time duration with respect to the original input. When PED functionality is targeted in the case of a packet-formatted input data signal, SOA-MZI delivers a single optical pulse at its S-port, with the pulse duration being similar to the duration of the entire original packet. In this application, line-rate information is completely ignored at the MZI output and only the packet-rate information can be identified at the output signal. On the other hand, when CR functionality is performed, the same SOA-MZI configuration yields a power-equalized clock pulse signal at its S-port, almost entirely removing the amplitude modulation of the clock resembling signal being inserted as the CTR signal. In this example, the data information originally carried by the input optical sequence has vanished at the SOA-MZI output and only the clock-rate information is retrieved at the S-port.

This multi-functional time-domain performance of the SOA-MZI-based configurations is inevitably correlated with different frequency domain characteristics for each of the system applications. Fig.9(c,d) depict the ideal frequency domain transfer function that should apply to the single SOA-MZI when PED or CR functions are performed by combining the preceded SOA-MZI WC operation with the subsystem of FPF. In the case of PED functionality shown in Fig. 9(d), all the data- and clock- information carrying frequency components have to be eliminated at the system's output and only the spectral content ranging from dc to the first packet-rate harmonic has to remain unaffected. This suggests

that the ideal PED transfer function has again to follow the characteristic curve of a low-pass filter but with a -3dB cut-off frequency not exceeding the value of the second packet-rate harmonic employed in the signal. This can be easily optimized by correctly tuning the SOAs gain, according to the analysis of Figure 5.
Finally, when CR functionality is intended, the complete spectral content of the original data signal except the clock-rate frequency harmonics has to be ignored. This indicates that the ideal CR circuit transfer function has to suppress the entire data spectral content and to exhibit periodic pass-bands only at the multiple clock-rate harmonics or at least at the first clock harmonic, as shown in Fig. 9(d).
PED and CR complete systems transfer function can be easily calculated by multiplying the theoretically obtained SOA-MZI frequency domain transfer function provided by equation (27) with the well known FPF's comb-like transfer function:

$$H_{PED/CR}(\omega) = H_{FPF}(\omega) \cdot H_{SOA-MZI}(\omega)$$

Fig. 10(a) depicts the FPF and the SOA-MZI response curves when gz=1 and t_{eff}=190psec, whereas Fig. 10(b) shows the respective graphs when gz=5 and t_{eff}=25psec. The total transfer function of the FPF-assisted SOA-MZI subsystem obtained through multiplication of the corresponding transfer functions of Fig. 10(a) and 10(b) are shown in Fig. 10(c) and 10(d), respectively. In order to be consistent with the experimental setups reported in (Kanellos et al, 2007), (Satmpoulidis et al 2007), in our theoretical analysis we have considered a 10 Gb/s 2^7-1 Pseudo-Random Bit Sequence (PRBS) optical signal with 10psec Gaussian pulses entering a FPF with a FSR equal to the bitrate and a finesse of 30.
Fig. 10(c) shows clearly that the complete spectral content has been suppressed by more than 15dB compared to the dc frequency component, allowing in this way only the spectral content residing within the bandwidth of the dc-centered resonance peak to emerge at the output. At the same time, Fig. 10(d) illustrates that the total transfer function retains the periodic FPF frequency characteristics suppressing, however, significantly the spectral content lying between dc and the first FPF harmonic. The effect of these transfer function curves on the original 10Gb/s PRBS data signal can be identified by transforming the data sequence into its Fourier-domain representation, multiplying this expression with the respective transfer function and then applying an inverse Fourier transform. The time-domain outcome of this procedure is depicted in Fig. 10(e) and 10(f) for the transfer functions of Fig. 10(c) and 10(d), respectively. Fig.10(e) shows a time-domain signal of almost constant amplitude confirming the effective elimination of the high-rate clock signal harmonics and the generation of the signal's low-rate envelope. This indicates that the proposed FPF-assisted SOA-MZI subsystem can lead to successful PED functionality when packet-formatted traffic is used by simply utilizing a 3-dB dc-peak bandwidth equal to the packet harmonic. Fig. 10(f) illustrates the time-domain signal obtained at the output of the SOA-MZI when the transfer function of Fig.10(d) is employed. As can be clearly identified, the initial PRBS data stream has been converted into a clock resembling signal with reduced amplitude modulation between its clock pulses, confirming the data harmonic suppression properties of the circuit and its effective use as a CR module.
PED and CR applications employ the same experimental setup, i.e. a FPF followed by a SOA-MZI switch that is powered by a CW beam as the input signal. This setup has been reported so far in experimental demonstrations to perform as a PED circuit (Stampoulidis et al 2007) when the SOAs are driven at low dc current values and as a CR circuit (Kanellos et

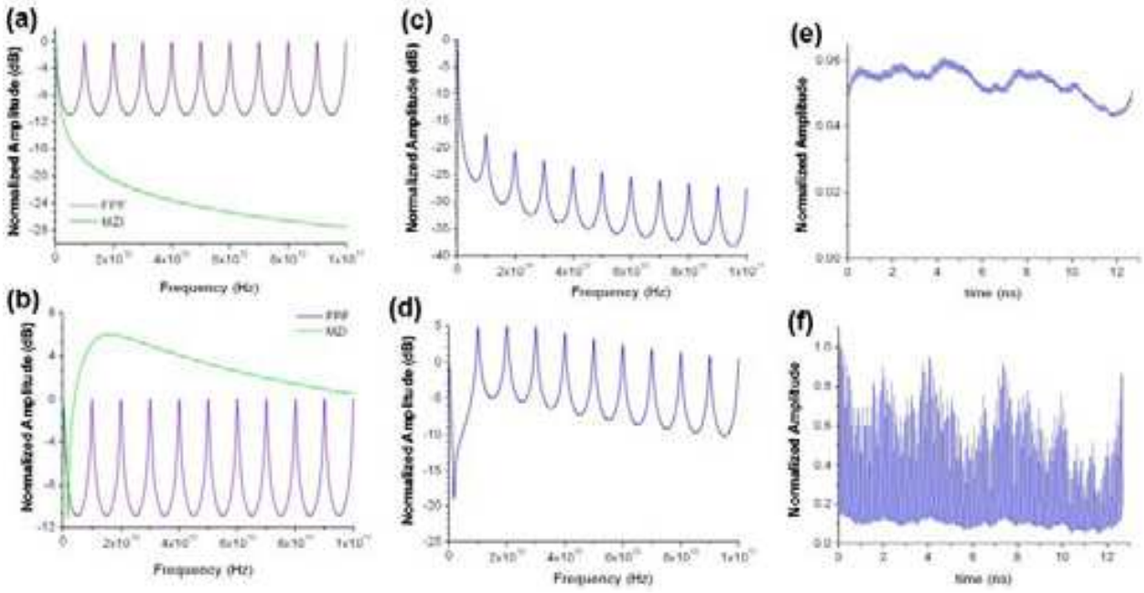

Fig. 10. (a), (b) Individual transfer functions of the FPF and SOA-MZI modules when gz=1, t_{eff}=190psec and gz=5, t_{eff}=25psec, respectively. (c), (d) corresponding total system transfer functions for the FPF-assisted SOA-MZI, and (e), (f) respective time-domain outputs when a 10Gb/s 2^7-1 PRBS input signal is employed.

al 2007) when the SOAs are operated in the saturated regime with moderate gain values and fast recovery speeds. This becomes evident if we consider the three SOA-MZI gain operational regimes discussed in Section 3.1. Low gain values for the SOAs yield the required low-pass filtering response required by a PED circuit that relies on a FPF-assisted SOA-MZI module. At the same time, the resonant behavior of the SOA-MZI at moderate SOA gain levels holds the credentials for supporting CR operation when placed after a FPF element, supporting the clock rate harmonics whilst suppressing the remaining spectral content. Finally, the smoother frequency dependence and the enhanced bandwidth arising when the SOAs are operating in their high gain regime render the circuit more suitable for WC applications, where a replica of the high-rate control signal has to be obtained at a new wavelength.

4. Conclusion

The theoretical frequency-domain transfer function of the SOA-MZI circuit and its qualitative verification even in more complex SOA-MZI-based subsystems allows for its exploitation in several functional applications yielding significant advantages in their theoretical performance analysis. A typical example is the use of cascaded SOA-MZI-based WC stages and its impact in terms of speed limitations and signal degradation due to accumulated jitter and amplitude modulation. This scenario can be now described for n cascaded WC stages by means of n-times multiplication of the single SOA-MZI transfer function, significantly improving the reliability and accuracy of the results compared to phenomenological transfer function descriptions that have been employed so far. Moreover, the SOA-MZI frequency domain transfer function enables the reliable theoretical proof-of-principle verification of more complex structures and applications that employ SOA-MZIs

as sub-elements, as long as the frequency response of the additional sub-modules is known. This can be of significant advantage in the case of novel photonic integrated circuitry where several configurations can be tested theoretically without necessitating the a priori circuit fabrication and its experimental evaluation.

5. References

Apostolopoulos, D.; Vyrsokinos, K.; Zakynthinos, P.; Pleros, N.; Avramopoulos, H. (2009a). An SOA-MZI NRZ Wavelength Conversion Scheme With Enhanced 2R Regeneration Characteristics, *IEEE Photon, Technol. Lett.*, Vol. 21, No. 19, 1363-1365, 1041-1135

Apostolopoulos, D.; Klonidis, D.; Zakynthinos, P.; Vyrsokinos, K.; Pleros, N.; Tomkos, I.; Avramopoulos, H.; (2009b). Cascadability Performance Evaluation of a new NRZ SOA-MZI Wavelength Converter, *IEEE Photon. Technol. Lett.*, Vol. 21, No. 18, 1341-1343, 1041-1135

Cao S.C. and J.C. Cartledge, "Characterization of the chirp and intensity modulation properties of an SOA-MZI wavelength converter"(2002), *J. of Lightwave Technol.*, vol. 20, pp. 689 - 695

Davies D.A.O., "Small-signal analysis of wavelength conversion in semiconductor laser amplifier via gain saturation",(1995) *IEEE Photon. Technol. Lett.*, vol. 7, pp. 617-619

Duelk, M.; Fischer, S.; Gamper, E.; Vogt, W.; Gini, E.; Melchior, H.; Hunziker, W.; Puleo, M.; Girardi, R.; (1999). Full 40 Gbit/s OTDM to WDM conversion: simultaneous four channel 40:10 Gbit/s all-optical demultiplexing and wavelength conversion to individual wavelengths, *Optical Fiber Communication Conference,* San Diego, CA , USA, ISBN: 1-55752-582-X, PD17/1 - PD17/3

Durhuus, T.; Joergensen, C.; Mikkelsen, B.; Pedersen, R.J.S.; and Stubkjaer, K.E. (1994). All Optical Wavelength Conversion by SOA's in Mach-Zehnder Configuration, *IEEE Photon, Technol. Lett.*, Vol. 6, No. 1, 53-55, 1041-1135

Fischer, S.; Bitter, M.; Caraccia, M.; Dülk, M.; Gamper, E.; Vogt, W.; Gini, E.; Melchior, H. and Hunziker, W., (2001). All-optical sampling with a monolithically integrated Mach–Zehnder interferometer gate, Optics Letters, Vol. 26, No. 9, 626–628, 0146-9592

Hill, M.T.; de Waardt, H.; Khoe, G. D. and Dorren, H. J. S. (2001). Fast optical flip-flop by use of Mach-Zehnder interferometers, *Microwave and Optical Technol. Lett.*, Vol. 31, No. 6, 411-415, 1098-2760

Kanellos, G.T.; Petrantonakis, D.; Tsiokos, D.; Bakopoulos, P.; Zakynthinos, P.; Pleros, N.; Apostolopoulos, D.; Maxwell, G.; Poustie, A.; Avramopoulos, H.; (2007a). All-Optical 3R Burst-Mode Reception at 40 Gb/s Using Four Integrated MZI Switches, *IEE/OSA J. Light. Tech.*, Vol. 25, No. 1, 184-192, 0733-8724

Kanellos G. T., et al, (2007b) "40 Gb/s 2R Burst Mode Receiver with a single integrated SOA-MZI switch", *OSA Optics Express*, Vol. 15, No. 8, pp. 5043-5049

Kim, J.Y.; Han S.K.; Lee, S., (2005) All-optical multiple logic gates using parallel SOA-MZI structures, *Lasers and Electro-Optics Society, 2005. LEOS 2005. The 18th Annual Meeting of the IEEE*, ISBN: 0-7803-9217-5, 133 – 134, October 2005, Paper MM1

Lal V., M. Masanovic, D. Wolfson, G. Fish, and D. Blumenthal (2006) "Monolithic Widely Tunable Packet Forwarding Chip in InP for All-Optical Label Switching," in

Integrated Photonics Research and Applications/Nanophotonics, Technical Digest (CD) (Optical Society of America, 2006), paper ITuC3.

Leuthold, J. (2001). Semiconductor Optical Amplifer-Based Devices for All-Optical High-Speed Wavelength Conversion. *Opt. Amplifiers and Their Applications Conf. (OAA'2001), Stresa, Italy, July 2001, paper OWA1*

Marcenac JD and A. Mecozzi, (1997) ''Switches and frequency converters based on cross-gain modulation in semiconductor optical amplifiers", *IEEE Photon. Technol. Lett.*, Vol. 9, pp. 749–751

Masanovic, M., Lal*,V.*, Barton*, J.S.*, Skogen*, E.J.*, Coldren*, L.A.*, and Blumenthal*, D.J.* (2003). Monolithically integrated Mach-Zehnder interferometer wavelength converter and widely tunable laser in InP, *IEEE Photon. Technol. Lett.*, vol. 15, No. 8, 1117-1119, 1041-1135

Maxwell, G.; (2006). Low-Cost Hybrid Photonic Integrated Circuits using Passive Alignment Techniques, invited paper MJ2, *IEEE-LEOS Annual Meeting*, Montreal, Canada (2006).

Melo A. Marques de , S. Randel, and K. Petermann,(2007)"Mach–Zehnder Interferometer-Based High-Speed OTDM Add–Drop Multiplexing", *J. of Lightwave Technol.*, vol. 25, no. 4, pp. 1017 – 1026

Nakamura, S.; Ueno, Y.; Tajima, K., (2001). 168-Gb/s all-optical wavelength conversion with a symmetric-Mach-Zehnder-type switch, *IEEE Photon. Technol. Lett.*, Vol. 13, No. 10, 1091-1093, 1041-1135

Nicholes, S.C.; Masanovic, M. L.; Jevremovic, B.; Lively, E.; Coldren, L.A. and Blumenthal, D.J. (2010). An 8x8 InP Monolithic Tunable Optical Router (MOTOR) Packet Forwarding Chip", *IEEE J. of Lightwave Technol.*, vol. 28, 641-650

Nielsen ML and J. (Mork,2004) "Increasing the modulation bandwidth of semiconductor-optical-amplifier-based switches by using optical filtering", *J. Opt. Soc. Am. B*, Vol. 21, pp. 1606-1619

Pleros N., C. Bintjas, G.T.Kanellos, K.Vlachos, H.Avramopoulos, G.Guekos (2004), Recipe for Intensity Modulation Reduction in SOA-Based Interferometric Switches *Journal of Lightwave Technology*, Vol. 22 , No. 12

Pleros N.; Apostolopoulos, D.; Petrantonakis, D.; Stamatiadis, C.; Avramopoulos, H.; (2009). Optical Static RAM Cell, *IEEE Photon, Technol. Lett.*, Vol. 21, No. 2, 73-75, 1041-1135

Ramaswami, R. & Sivarajan, K.N. (2002). *Optical Networks: a Practical Perspective,* R. Adams Editor, Second Ed., Morgan Kaufmann Publisher, ISBN 1-55860-655-6, USA

F. Ramos et al. (2005) IST-LASAGNE:Towards All-Optical Label Swapping Employing Optical Logic Gates and Optical Flip-Flops *Journal of Lightwave Technology*, Vol. 23 , No. 10

Stampoulidis, L.; Kehayas, E.; Apostolopoulos, D.; Bakopoulos, P.; Vyrsokinos, K.; Avramopoulos, H.; (2007). On-the-Fly All-Optical Contention Resolution for NRZ and RZ Data Formats Using Packet Envelope Detection and Integrated Optical Switches, *IEEE Photon, Technol. Lett.*, Vol. 19, No. 8, 538-540, 1041-1135

Stampoulidis, et al (2008). Enabling Tb/s Photonic Routing: Development of Advanced Hybrid Integrated Photonic Devices to Realize High-Speed, All-Optical Packet Switching, *IEEE J. of Sel. Topics in Quantum Electron.*, Vol. 14, No. 3, 849 – 860, 1077-260X

Stubkjaer, K.E. (2000). Semiconductor Optical Amplifier-Based All-Optical Gates for High-Speed Optical Processing. *IEEE J. on Selected Topics in Quantum Electronics,* Vol. 6, No. 6, (November/December 2000), 1428-1435, 1077-260X

Ueno, Y.; Nakamura, S.; Tajima, K. (2001). Penalty-free error-free all-optical data pulse regeneration at 84 Gb/s by using a symmetric-Mach-Zehnder-type semiconductor regenerator, *IEEE Photon. Technol. Lett.*, vol. 13, No. 5, 469-471, 1041-1135

Wang, L.; Zhang, M.; Zhao, Y.; Ye, P. (2004). Performance analysis of the all-optical XOR gate using SOA-MZI with a differential modulation scheme, *Microwave and Opt. Tech. Lett.,* Vol. 40, No. 2, 173-177, 1098-2760

Webb, R.P.; Manning, R.J.; Maxwell, G.D.; Poustie, A.J. (2003). 40 Gbit/s all-optical XOR gate based on hybrid-integrated Mach-Zehnder interferometer, *Electron. Lett.* Vol. 39, No. 1, 79-81, 0013-5194

Wolfson, D.; Kloch, A.; Fjelde, T.; Janz, C.; Dagens, B. and Renaud, M. (2000). 40-Gb/s All-Optical Wavelength Conversion, Regeneration, and Demultiplexing in an SOA-Based All-Active Mach–Zehnder Interferometer, *IEEE Photon, Technol. Lett.*, Vol. 12, No. 3, 332-334, 1041-1135

Yan N., J. del Val Puente, T.G. Silveira, A. Teixeira, A.P.S. Ferreira, E. Tangdiongga, P. Monteiro and A.M.J. Koonen, 2009 "Simulation and experimental characterization of SOA-MZI-based multiwavelength conversion", *IEEE J. of Lightwave Technol.*, vol. 27, No. 2, pp. 117 – 127

Zakynthinos, P.; Kanellos, G.T.; Klonidis, D.; Apostolopoulos, D.; Pleros, N.; Poustie, A.; Maxwell, G.; Tomkos, I.; Avramopoulos, H.; (2007). Cascaded operation of a 2R Burst Mode Regenerator for Optical Burst Switching network transmission, *IEEE Photon. Technol. Lett.*, Vol. 19, No. 22, 1834-1836, 1041-1135

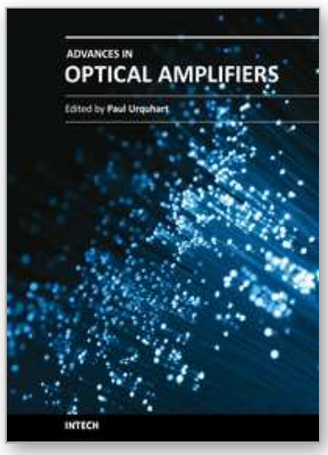

Advances in Optical Amplifiers
Edited by Prof. Paul Urquhart

ISBN 978-953-307-186-2
Hard cover, 436 pages
Publisher InTech
Published online 14, February, 2011
Published in print edition February, 2011

Optical amplifiers play a central role in all categories of fibre communications systems and networks. By compensating for the losses exerted by the transmission medium and the components through which the signals pass, they reduce the need for expensive and slow optical-electrical-optical conversion. The photonic gain media, which are normally based on glass- or semiconductor-based waveguides, can amplify many high speed wavelength division multiplexed channels simultaneously. Recent research has also concentrated on wavelength conversion, switching, demultiplexing in the time domain and other enhanced functions. Advances in Optical Amplifiers presents up to date results on amplifier performance, along with explanations of their relevance, from leading researchers in the field. Its chapters cover amplifiers based on rare earth doped fibres and waveguides, stimulated Raman scattering, nonlinear parametric processes and semiconductor media. Wavelength conversion and other enhanced signal processing functions are also considered in depth. This book is targeted at research, development and design engineers from teams in manufacturing industry, academia and telecommunications service operators.

InTech Europe
University Campus STeP Ri
Slavka Krautzeka 83/A
51000 Rijeka, Croatia
Phone: +385 (51) 770 447
Fax: +385 (51) 686 166
www.intechopen.com

InTech China
Unit 405, Office Block, Hotel Equatorial Shanghai
No.65, Yan An Road (West), Shanghai, 200040, China
中国上海市延安西路65号上海国际贵都大饭店办公楼405单元
Phone: +86-21-62489820
Fax: +86-21-62489821

IntechOpen